Jurnal Teknologi

Full Paper

GAMMA RADIATION SHIELDING POTENCY OF B_2O_3–TeO_2–BaO–Dy_2O_3 GLASS-CERAMIC

Saba Farhan HATHOT[a], Balqees Mohameed AL-DABBAGH[a]
Haydar aboud[b]

[a]Applied Science Dep, University of Technology,10066 Baghdad, Iraq
[b]College of sci., Al-Mustansiriya University, Iraq

Article history
Received
21 May 2024
Received in revised form
7 August 2024
Accepted
26 August 2024
Published Online
26 June 2025

*Corresponding author
as.21.25@grad.uotechnology.edu.iq

Graphical abstract

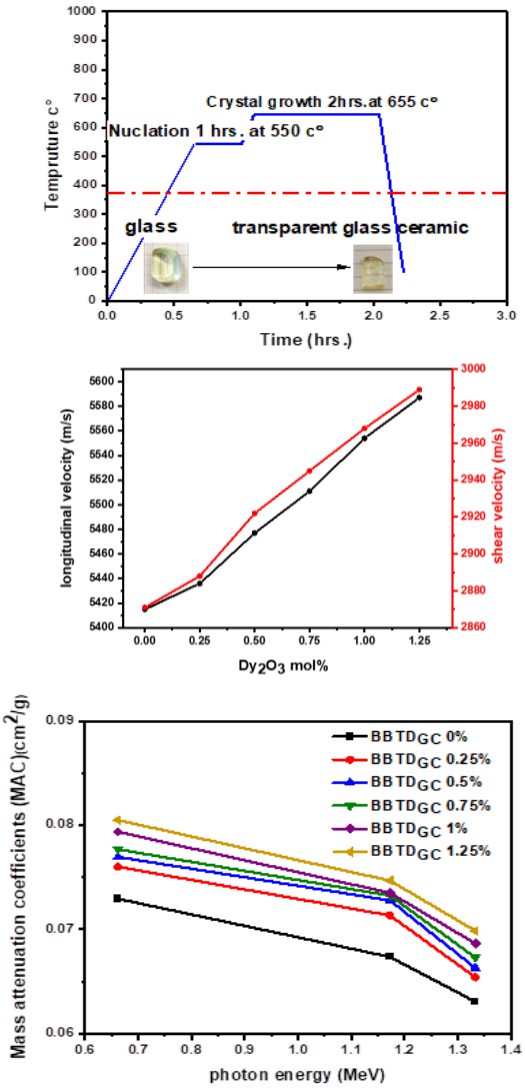

Abstract

Ionizing radiation Teletherapy Ionizing radiation is used in medical imaging, radiation therapy and research, which requires high-performance shielding materials to be safe. Ionizing radiations are very dangerous to the health and this is dependent on the amount of dose and the duration of exposure. Considering this, it is important to develop shielding materials. In this work, a novel family of glass systems was synthesized (50-x)B 2 O 3 -25TeO 2 -25BaO-xDy 2 O 3 with 0 mol % x 1.25 mol %. Partially crystallized glass ceramic (GC) samples were obtained by undergoing a stepwise heating processing: annealing at 570 0 C and heating at 6201655 0 C for 2 hours forming glasses. XRD structural analysis proved crystallinity as well as multi-phased. High Dy 2 O 3 content also increased the G C density to 4.994 g / cm 3 and reduced molar volume to 24.8376 cm 3 / mol as well as led to a rise in elastic properties such as longitudinal velocity, shear velocity, longitudinal elastic modulus and shear elastic modulus as a reflection of the increased density and bond strength. The shielding effectiveness of gamma rays against sources of 137Cs and 60Co at 0.662, 1.173, and 1.333 MeV were tested by a NaI(Tl) detector. As concentration of Dy2O 3 increased, the mass attenuation coefficient (MAC) increased in this order BBTDGC1.25 > BBTDGC1 > BBTDGC0.75 > BBTDGC0. The BBTDGC1.25 sample had the best MAC and worst half-value layer (HVL) tenth-value layer (TVL) and mean free path (MFP), which are better against gamma-ray shield. Therefore BBTDGC1.25 glass ceramic has a good prospect as a good gamma radiation shielding agent in comparison to the other samples provided.

Keywords: Glass-ceramic, MAC, HVL, TVL, MFP, Shielding

1.0 INTRODUCTION

Through the controlled crystallization of glass, composite materials known as glass-ceramics are formed, showing characteristic fine grains and homogeneous structures. This structure is composed of small crystals that have an irregular and distorted shape, wherein these tiny grains are often grouped together in spheroids, with residual glass inter-layers that bind the GC concretion [1].The expected outcome of these materials is that they will possess good mechanical, electrical, and thermal properties, along with a high level of chemical durability and an extremely low coefficient of thermal expansion when compared to glass [2, 3]. The crack growth in these materials is further impeded by the inter-wined crystals that are present. Consequently, the studies focusing on crystallization and its relationship with the physical properties [4]. The GC materials have gained significant interest in various industrial and engineering applications due to their advantageous properties [5]. Tellurite with boron oxide glass systems doped with (rear earth elements) have unique optical and electronic properties[6]. Rare-earth (RE) ions are interesting elements due to their unique properties, particularly in the field of optical and photonic devices [6]. Glasses doped with dysprosium oxide (Dy_2O_3) can exhibit enhanced optical and magnetic properties, making them suitable for various applications [7, 8]. Tellurite glasses are considered excellent hosts for the RE ions due to their low phonon energy of approximately 700 cm^{-1}. This characteristic allows for the effective inhibition of non-radiative processes, leading to improved quantum efficiencies [9, 10]. During the process of crystallization, nucleating agents such as RE ions have the ability to either facilitate the separation of different phases or contribute to the accumulation of specific micro- or nano-phase within the phase separated glasses [11].

The conventional method of heat treatment is utilized to create a crystalline environment in glasses that involves the nucleation steps and subsequent growth of crystals. This created a possibility to produce GC materials with nanocrystals of sizes below 100 nm. These materials have unique characteristics (like enhanced thermal stability, electro-optic effects, and elastic modulus) different from the original glass [5]. These properties make them suitable for engineering a wide range of technical and household appliances [12] Ionizing radiation is an essential technology that plays a crucial role in medicine, energy, safety, diagnostics, and resource exploration. However, it is absolutely necessary to handle radiation sources safely, as there is no completely risk-free level of exposure to radiation [13]. In the field of medicine, radiation is heavily utilized for tasks such as X-ray imaging and radiation therapy, which are employed to shrink or eradicate tumors. Radioisotopes are also employed in the agricultural industry to induce mutations in crops [14]. Researchers have discovered that rare earth elements can be effectively used as doping materials in glass, resulting in numerous benefits derived from their exceptional properties, Siripuram and co-workers [12] made some tellurite glass and glass-ceramic systems, containing Nb_2O_5 and Comparative studies of the structural, optical and thermal properties of glass and glass-ceramic systems have been systematically performed. The physical properties reveal that the formation of a glass network is associated with a less dense and less compact structure due to the degradation of structural units by the formation of non-bridging oxygen sites in the glass matrix. However, glass-ceramic systems exhibit an increase in average bond energy, increased density, a shift in the system to close packed and more compactness state, and a decrease in the optical edge and refractive index with an increase in the band gap. Imed Boukhris et al; [13] studied the Chalcogenide glass-ceramics containing $xCsCl-(100-x)(0.5GeS_2-0.5Sb_2S_3)$ show promising radiation shielding properties. The mass attenuation coefficient (μ/ρ), half value layer (HVL), removal cross section (RCS), exposure buildup factor (EBF), mean free path (MFP), and effective atomic number (Zeff) were analyzed to understand how well the chalcogenide glass-ceramics can shield radiation. The μ/ρ values of Geant4 simulations and theoretical calculations showed a strong agreement. The clear indication of low EBF values, particularly at lower and intermediate photon energies, supports the potential application of the suggested glasses for shielding purposes in medical contexts. Over the past ten years, one of the hidden objectives of numerous research groups has been the pursuit of materials with dual functionalities [15]. Nevertheless, there are ways to develop materials that can lessen radiation across various energy levels, and the choice of materials with suitable high densities plays a crucial role in this [16]. Both glasses and glass ceramics have the ability to function as transparent materials while also blocking radiation [17, 18]. Glasses and glass ceramics have gained significant attention in this industry due to their many advantages, such as easy manufacturing, cleanliness, clarity, light transparency, and portability [1]. Glasses are often made by combining two or more components. The composition of the glass and glass ceramic is determined based on the intended application. The presence of crystalline phases and grain structure in glass ceramics gives them the ability to exhibit a range of transparency, from clear to opaque. Glass ceramics can range from highly crystalline to containing a substantial amount of glass [19]. Glass formers and modifiers can thus be used to change the features of glasses associated with physical and structural needs [20]High-density glass formers play a vital role in the structure of glass, making them indispensable for creating a shield that is highly effective. Glass can be made by using different glass formers such as B_2O_3, TeO_2, SiO_2, P_2O_3, and GeO_2 [21, 22]. Adding metal oxides and rare earth in specific ratios to the glass matrix can improve its physical properties, including radiation shielding [23]. The primary focus of this work is to synthesize TeO_2-based barium-borate glasses and GC with Dy_2O_3 doping at various contents. Glass samples were converted into GC using the traditional heat treatment process, leading to 2 step

mechanisms such as nucleation and crystal growth. The effects of various Dy_2O_3 doping contents on the hardness, density, structures, and gamma radiation shielding traits of the obtained GC were studied, displaying their excellent promise towards the attenuation of gamma rays.

2.0 METHODOLOGY

The new glass system composed of (50-x) B_2O_3-25TeO_2-25BaO-x$Dy_2O_3$with x = 0, 0.25, 0.5, 0.75, 1 and 1.25 mol% was prepared by the melt-quenching approach.Once the chemical powders were measured, combined, and stirred, the mixture was transferred into a platinum crucible.This crucible, along with its contents, was then placed inside an electric furnace set at a temperature of 950 °C for the duration of 30 minutes to ensure complete melting. A separate furnace was used to conduct the annealing process, which lasted for three hours at a temperature of 350 °C preparation of glass sample show in Figure 1. The DTA analysis of the samples was conducted from room temperature up to 900 °C, with a heating rate of 10 °C/min. The purpose of this analysis was to determine the temperature of glass transition T_g , crystallization onset (T_x), and crystallization (T_c). To produce a glass-ceramic, first the glasses were prepared. Next, these glasses were partially crystallized through a controlled heat treatment at two phases like annealing for 1 h (at 570 °C) and heating for 2 h in the range of 620-655 °C preparation glass ceramic sample preparation show in Figure 2. The GC samples made with of Dy_2O_3 contents of 0, 0.25, 0.5, 0.75, 1, and 1.25 mol% were named as $BBTD_{GC}0$, $BBTD_{GC}0.25$, $BBTD_{GC}0.5$, $BBTD_{GC}0.75$, $BBTD_{GC}1.0$, and $BBTD_{GC}1.25$. The obtained GC samples were characterized at room temperature by various measurement tools including XRD, FESEM, DTA, etc.

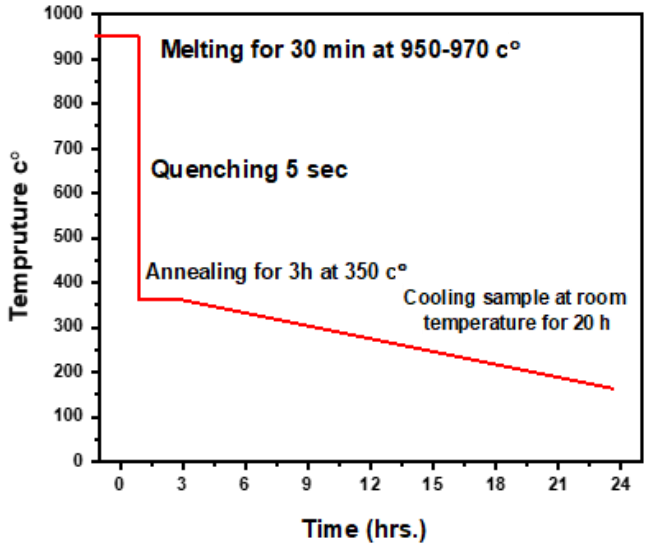

Figure 1 The diagram of the glass sample preparation

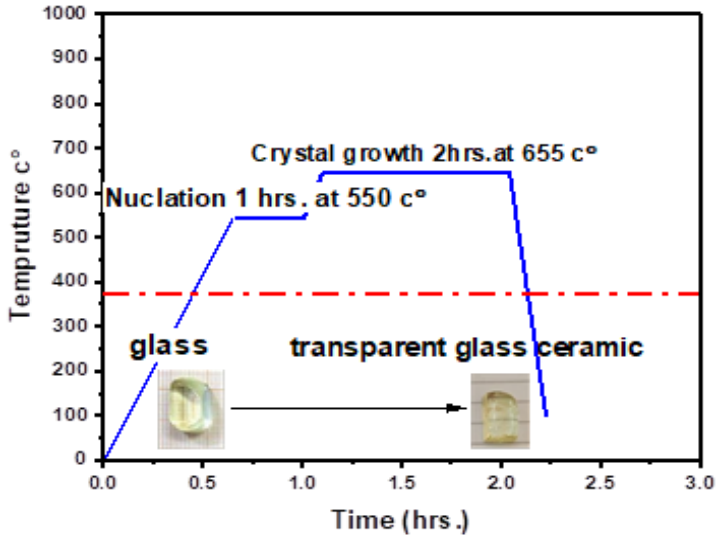

Figure 2 The diagram of the glass ceramic sample preparation

3.0 RESULTS AND DISCUSSION

3.1 Structure and Morphology Analysis of GC

Figure 3 displays the XRD profiles of the glasses, sowing a broad hump centered around 25°, which highlights the asymmetric nature of the crystals present. To induce the crystal formation the glasses were subjected to specific temperature regimes determined from DTA thermograms. For every sample the crystallization required a different temperature and time duration, depending on the temperature parameters obtained from the thermograms. This controlled heat treatment results in the formation of distinct crystalline peaks in the XRD profiles. The sharp peak signifies the presence of well-defined crystal planes, while the wider hump indicates the presence of amorphous regions or less ordered structures within the glass ceramic samples.

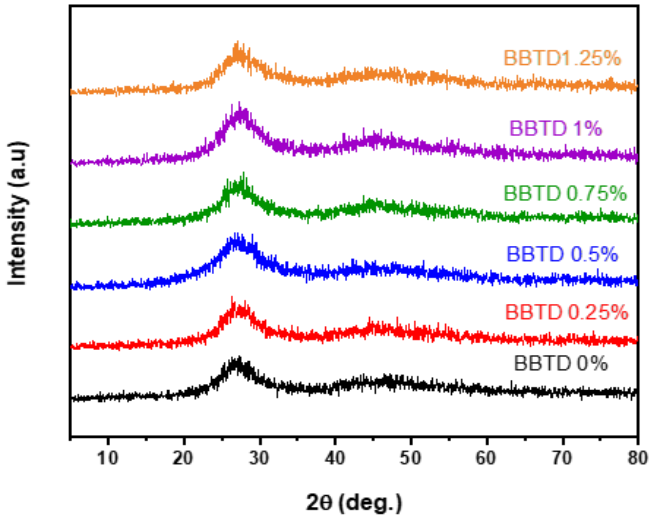

Figure 3 XRD profiles of the glasses

The XRD peaks in Figure 4 shows the nano crystallinity in the obtained GC that superimposed on the diffuse background of the host glass. The XRD patterns of the GC annealed at 520 ^{0}C for 1 h and then at 600 ^{0}C for 2 h clearly showed the nucleation and growth process. The intense crystalline peaks shown by BBTD$_{GC}$0 sample was identified as orthorhombic $B_2Ba_3O_6$(112), cubic TeO_2O_5 (003), Cubic TeO_2 (011), Cubic B_2O_3 (101) and Tetragonal BaO_2(101), which were matched with the corresponding JCPDS card number of [96-154-8109], [96-145-0090], [96-154-8797], [96-151-0797] and [96-901-3414]. The mean size of grain in this sample was 17 nm.

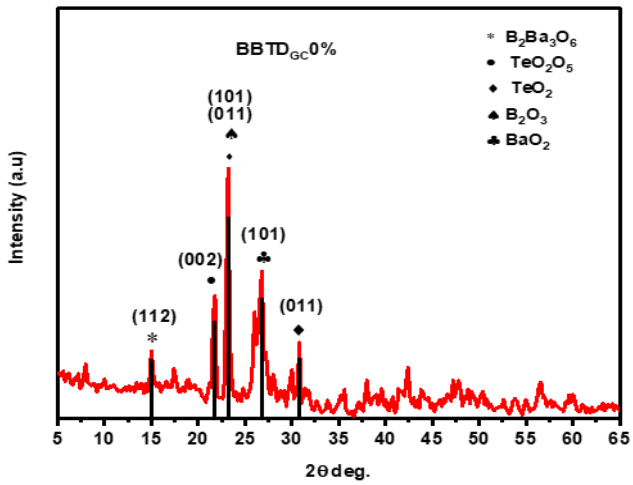

Figure 4 XRD patterns of BBTT$_{GC}$ 0% sample annealed at 520-600 ^{0}C for 3hrs

Figure 5 showed three different crystal structures such cubic TeO_2 (011)Cubic B_2O_3 (101) and triclinic $Ba_3Te_4O_{11}$ (021) that tallied with the corresponding JCPDS card number of [96-145-0090], [96-154-8797], and [96-202-0150].

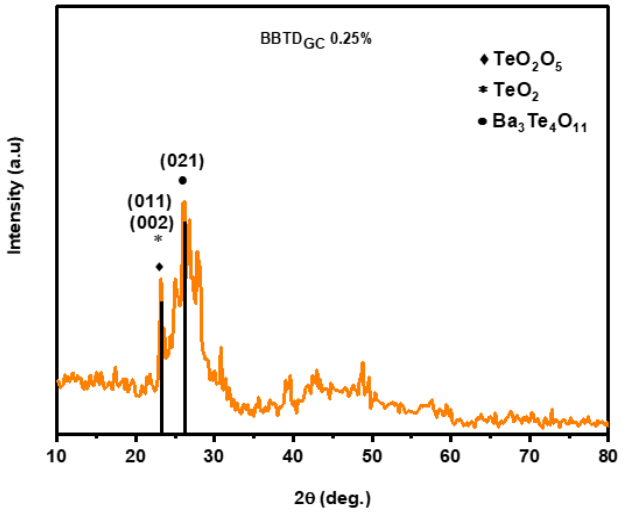

Figure 5 XRD patterns of BBTT$_{GC}$ 0.25% sample annealed at 550-612 ^{0}C for 3hrs

BBTT$_{GC}$0.5 and BBTT$_{GC}$0.75 sample annealed at 550 °C for 1 h and then 633 °C for 2 h as shown in Figures 6&7 respectivly displayed 5 distinct crystalline structures like cubic TeO_2O_5(003), cubic TeO_2(011), trigonal TeO_3(110), triclinic $Ba_3Te_4O_{11}$(021), and hexagonal BDy_2O_3(440) that corresponded to the JCPDS card number of [96-210-7045], [96-154-8797], [96-153-5877], [96-202-0150], and [96-151-1090] having gain size range of 12.6-13.6.

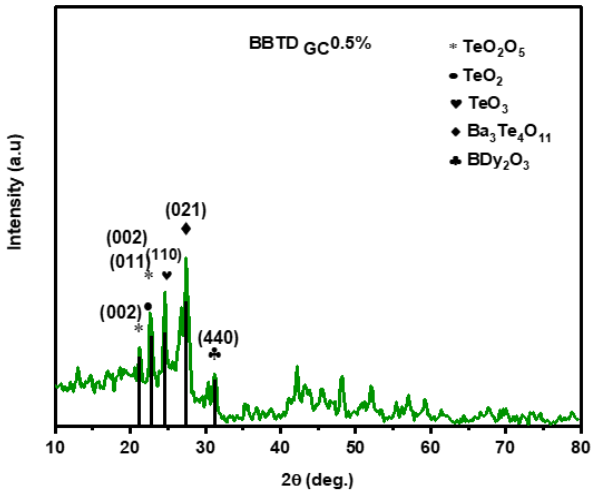

Figure 6 XRD patterns of BBTT$_{GC}$ 0.5% sample annealed at 550-633 ^{0}C for 3hrs

Figure 7 showed four different distinct crystalline structures with crystalline size of 42 nm.**C**rystal phase including cubic TeO_2 (011), trigonal TeO_3 (110), triclinic $Ba_3Te_4O_{11}$ (021), hexagonal BDy_2O_3 (440) and triclinic Dy_2O_2Te (013) corresponding to the JCPDS card number of [96-210-7045], [96-154-8797], [96-202-0150], and [96-151-1090].

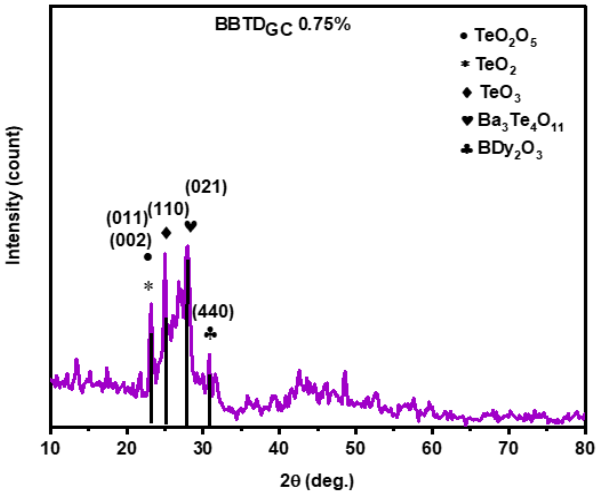

Figure 7 XRD patterns of BBTTGC 0.5% sample annealed at 550-633 ^{0}C for 3hrs

Figure 8 showed four different distinct crystalline structures with crystalline size of 48 nm exhibited crystal phase TeO_2 (011), trigonal TeO_3 (110), $Ba_3Te_4O_{11}$ (021), hexagonal BDy_2O_3 (440) and triclinic Dy_2O_2Te (013) corresponding to the JCPDS card number of [96-154-8797], [96-153-5877], [96-202-0150], [96-151-1090],and [96-210-7045]. The grain size was calculated by Debye-Scherrer formula [24]:

$$T = \frac{K\lambda}{A\cos(\theta)} \quad (1)$$

Where λ is the wavelength of the x-ray, and β is width (in radians) of the peak at 2θ. The samples were also stack the data in the Figure10.

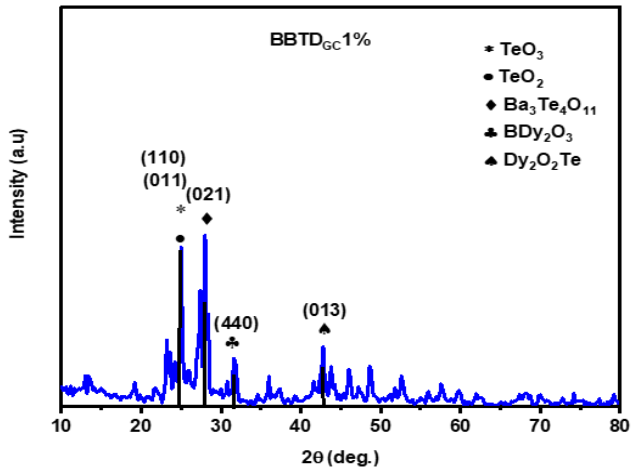

Figure 8 XRD patterns of BBTT$_{GC}$ 1%sample annealed at 550-646 ^{0}C for 3hrs

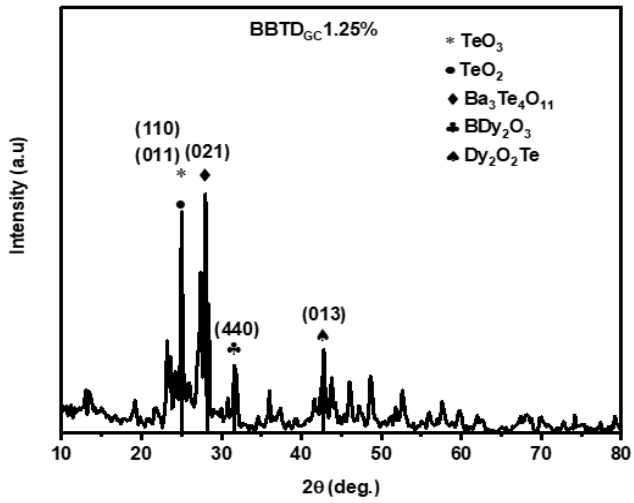

Figure 9 XRD patterns of BBTT$_{GC}$1.25% sample annealed at 550-646 0C for 3hrs

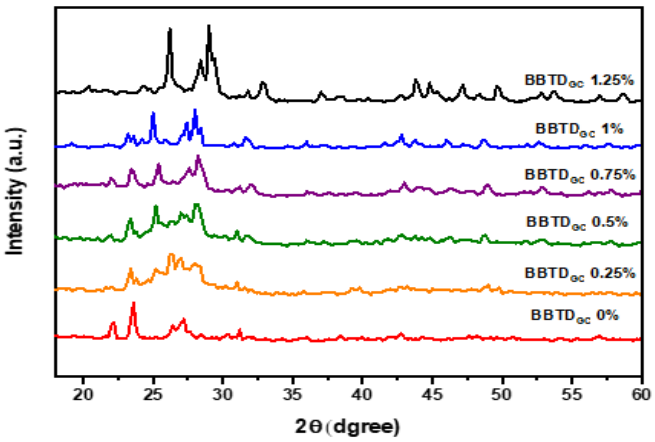

Figure 10 XRD patterns of all BBTT$_{GC}$ sample annealed with different temperature

By using field emission scanning electron the microstructure of samples was studied for cross-section images of the studied nano-powder samples: BBTD$_{GC}$ 0, BBTD$_{GC}$ 0.25, BBTD$_{GC}$ 0.5, BBTD$_{GC}$ 0.75, BBTD$_{GC}$1 and BBTD$_{GC}$1.25 showed in Figure 4.11. Instead of chemical treatment, the surface of the samples was coated with a thin layer of gold film. The powder samples BBTD$_{GC}$ 0 and BBTD$_{GC}$ 0.25 exhibited grains with sharp edges that were visibly accumulated, unlike the other samples. The edges of these grains were well-defined and angular, indicating a higher degree of aggregation. This aggregation could be attributed to the presence of low concentration of Dy_2O_3 additives or processing conditions during the production of BBTD$_{GC}$ 0 and BBTD$_{GC}$ 0.25. The addition of Dy_2O_3 to the pure powder of sample resulted in a significant change in the surface morphology. The presence of Dy_2O_3 seems to have influenced the formation of smaller, nearly spherical grains. These grains appear to contain accumulated nanoparticles, which can be observed on the surface. Interestingly, some nano-rods are still observed within these smaller grains, suggesting a complex interaction between the Dy_2O_3 and the nanoparticles. This finding highlights the potential role of Dy_2O_3 as a modifier in controlling the morphology and structure of doped samples.

Two magnifications (5 and 1 µm) were used to get the samples FESEM images Figure 11. Instead of chemical treatment, A thin layer of gold film was applied to the surface of the samples. The BBTD$_{GC}$0% & BBTD$_{GC}$0.25% GC exhibited grains with sharp edges that were visibly accumulated, unlike the other samples. The morphology of the particles displayed differences in form. The edges of these grains were well-defined and angular, indicating a higher degree of aggregation. This aggregation could be attributed to the presence of low concentration of Dy_2O_3 additives or processing conditions during the production of BBTD$_{GC}$0 & BBTD$_{GC}$0.25 samples. The surface texture of the sample underwent a significant transformation when Dy_2O_3 was incorporated into the pure powder. It appeared that the introduction of Dy_2O_3 and the utilization of higher heat treatment had an influence on the formation of

grains, resulting in their smaller size and more spherical morphology. The grains that were examined seemed to contain nanoparticles that had clumped together, and these aggregates were visible on the surface. By highlighting the potential role of Dy_2O_3, this finding emphasizes its ability to act as a modifier and exert control over the morphology and structure of the doped samples. The formation of nanoparticles with various shapes within the random glass matrix is heavily influenced by heat treatment and temperature control. This, in turn, results in the production of denser and more interconnected samples, ultimately enhancing their mechanical properties and ability to attenuate high gamma rays. The analysis revealed that the majority of particles in the sample had sizes ranging from 40 to 70 nm.

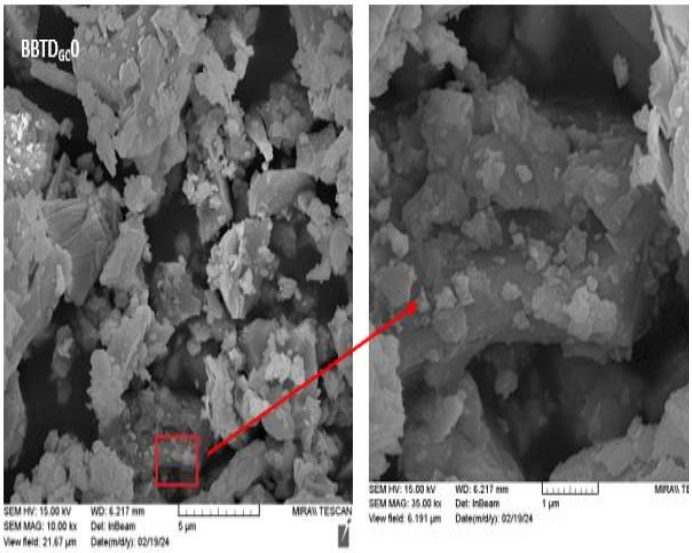

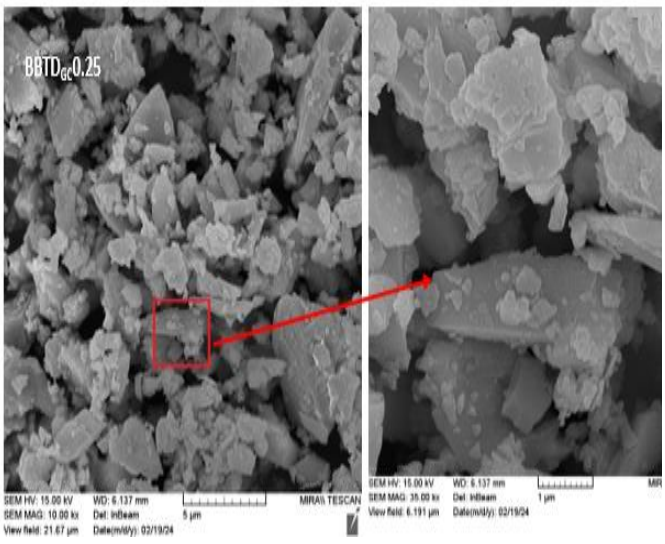

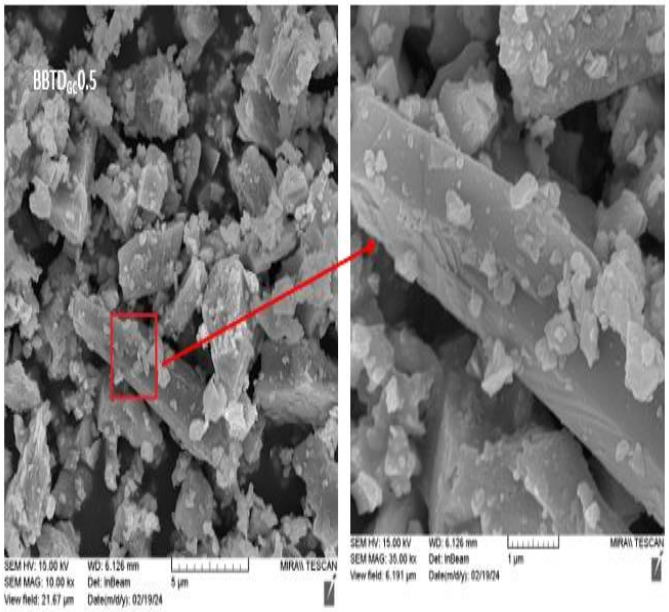

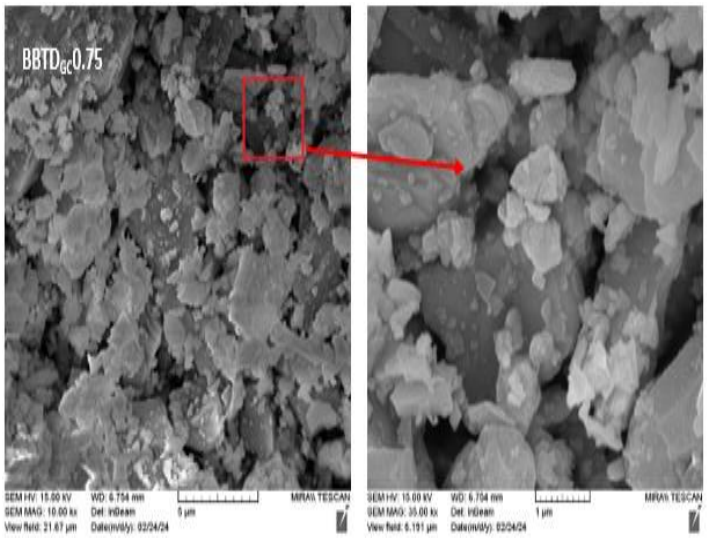

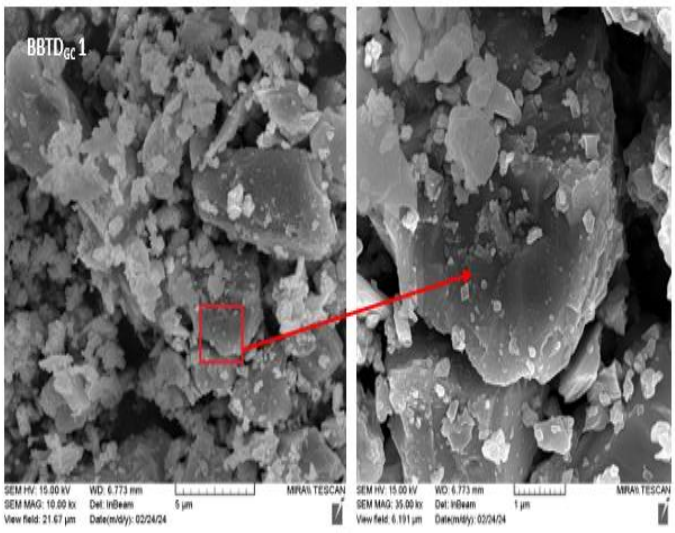

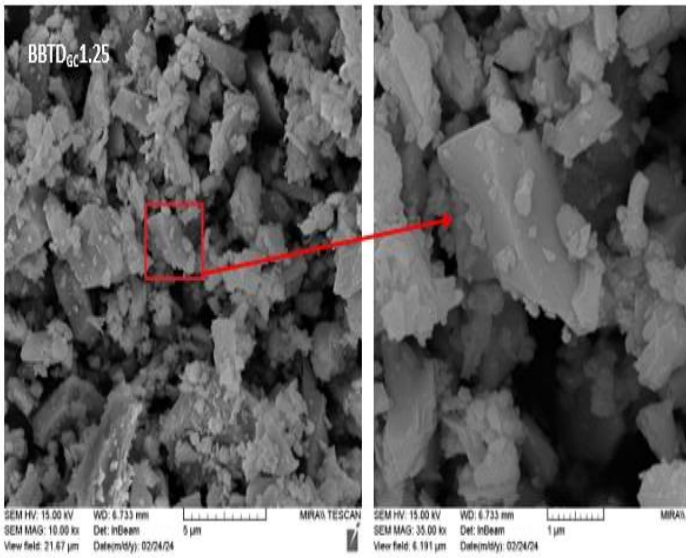

Figure 11 FESEM images of the made GC at different magnification

3.2 Physical Characteristics of GC

Figure 12 displays the obtained densities, molar volumes, and oxygen packing densities (OPD) of the GC, wherein the densities were increased from 4.66 - 4.795 gm/cm^3 as Dy_2O_3 concentration was increased. The increase of density was mainly due to the high packing of structural units when replacing B_2O_3 by Dy_2O_3. The density of the GC is significantly higher than that of the glass system due to its increased compactness [25]. The density was determined using the following equation:

$$\rho = \frac{W_a}{W_a - W_l} \times \rho_{\text{fluid}} \quad (2)$$

Where Wa the weight of the sample in air, Wl the weight of the sample in toluene.

The addition of Dy_2O_3 caused a decrease in the molar volume of GC from 25.777 - 24.837 cm^3/mol. Variations in the distance between atoms resulted in alterations in the volume of one mole of substance due to modifications in its structure when the glass transformed into GC, the increased cross-linkages of the network results in higher OPD values for the GC compared to the glass. This suggested that the increased cross-linkages might have contributed to the higher OPD values observed in glass-ceramic systems [26]. The samples OPD was determined using [27]:

$$OPD = \frac{1000 \times N}{V_m} \quad (3)$$

Where, N is the number of oxygen atoms per formula unit, V_m molar volume.

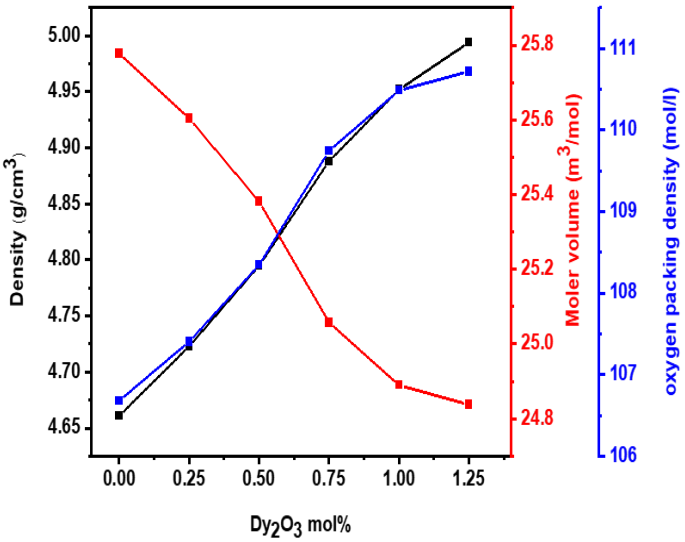

Figure 12 Density, molar volume, and OPD of GC with varying Dy2O3 concentrations

3.3 Thermal Properties of GC

The thermal properties of the samples were analyzed using a DTA instrument, specifically the Pyries Diamond TG.DTA from Japan, with a heating rate of $10C^{\circ}$/min. A broad endothermic peak was observed in the obtained DTA curves Figure 13, which can be attributed to glass transition Tg. Subsequent to this transition, there occurred an additional endothermic event, which was found to be related to , crystallization temperature Tc. Lastly, the other endothermic event was observed, corresponding to melting temperature Tm via the equation thermal stability $S = (TC - Tg)$.

The calculated Hruby parameters of the GC are shown in Table 1. The increase in the amount of host rare earth (RE) in the glassy network enabled to strengthen the stretching force constant of bonds. This results in a decrease in inter-atomic spacing, causing the macromolecular structure to become more closely packed. As the molecules become tightly packed, more energy is required to overcome the intermolecular forces and attain the necessary mobility for the glass transition. This increased energy requirement leads to a higher Tg. In other words, as the amount of host rare earth increases, the glassy network becomes more rigid and requires more energy to convert from a solid to a glassy state. Thus, the change of Tg was due to the change of molar volume and inter-atomic distances that are affected by the stretching force constant and OPD in the glass matrix [28]. The primary reason for the increase in the Tg with the presence of RE ions is the enhanced connectivity of the network. This is attributed to the fact that the bond strength between the host and oxygen is higher compared to that of tellurium and oxygen bonds. Consequently, the Tg of the samples is elevated. The weak covalent bonds of Te-O-Te bridges are substituted with strong O-RE ionic bonds. The presence of a strong electrostatic field from the ionic

bonds contributes to the increase in both Tg and Tm value of the GC [29] .

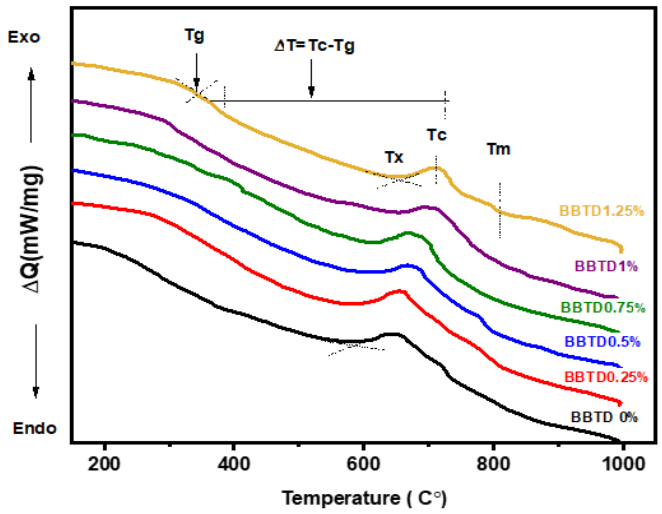

Figure 13 DTA results of the GC

With increasing Dy_2O_3 contents, there is also an increase in the value of Tc [30].The values of S and Tc serve as indicators of the glass's ability to form easily [31]. The observed increases in these parameters suggest that the RE ions could be effective glass modifiers. The glass structure can be effectively strengthened by altering the TeO_4 tbp unit to a TeO_3 tp unit and coordinating it with TeO_{3+1} [32]. The thermal stability (S)as well as the Hruby's parameter H together with the glass-forming tendency, clearly indicate a strong propensity for good glass formation and stability [33] [34].

Hruby's parameter (H)[35]. This parameter serves as a valuable measure for assessing the devitrification tendency of the glass samples.

$$H = \frac{T_c - T_g}{T_m - T_c} \quad (4)$$

The T_g/T_m ratio of the glass transition and melting temperatures factor is a useful tool for evaluating glass stability [36].

Table 1 Glass transition **Tg**, onset crystallization temperature **Tx**,crystallization temperature (onsetpoint) **Tc**,melting temperature **Tm**, thermal stability temperature **S** ,Hurby's parameter **H**,and **Tg/Tm** ratio of glasses samples

Sample code	Tg c°	Tx c°	Tc c°	Tm c°	S c°	H	Tg/Tm
BBTD0%	265	598	646	729	381	4.59036	0.41021
BBTD 0.25%	274	616	660	789	386	2.99224	0.41515
BBTD0.5%	292	630	672	792	380	3.16666	0.43452
BBTD0.75%	301	639	674	798	373	3.00806	0.44658
BBTD1%	313	648	704	805	391	3.87128	0.44460
BBTD1.25%	342	658	711	810	369	3.72727	0.48101

3.4 Mechanical Properties of GC

Figure 14 display the estimated value of longitudinal vl and shear velocity vs of GC was improved with the increase of Dy_2O_3 contents. this increase indicated rise the internal energy [37]. In order to calculate elastic modules of the GC as:

$$\mathrm{L} = \rho(\upsilon_\mathrm{l})^2 \quad (5)$$
$$\mathrm{G} = \rho\upsilon_\mathrm{s}{}^2 \quad (6)$$
$$\mathrm{K} = \mathrm{L} - \frac{4}{3}\,\mathrm{G} \quad (7)$$
$$\mathrm{E} = (1+\sigma)2\mathrm{G} \quad (8)$$

Where L longitudinal modulus, G shear modulus, K bulk modulus,and E youngs modulus.

The elastic modulus of glass-ceramic materials was estimated and is depicted in the Figure 15. It was discovered that Dy_2O_3 ,and increasing heat treatment contributes to the increase in these velocities due to its impact on density, bonding strength, and cross-link density [37]. "Poisson's ratio σ ", "microhardness H", "thermal expansion coefficient α_p", and "Debye temperature θ_D" of the GC depicted in Table 2 were increased with increase Dy_2O_3 content this evidence strongly supports the presence RE dopants in the glass system due to the forming of BOs, resulting in a more compact glass network due to the changeain structural units[38] by ingreasing heat treatment the glass ceramic becomes more rigid as a result of increased networking between the atoms in addition to increasing the BOs number [39].

Poisson's ratio: $\sigma = \frac{(L-2G)}{2(L-G)}$ (9)

Microhardness: $H = \frac{(1-2\sigma)E}{6(1+\sigma)}$ (10)

Thermal expansion coefficient: $\alpha_\mathrm{p} = 23.2(\mathrm{v_l} - 0.5745)$ (11)

Debyetemperature: $\theta_D = \frac{h}{k}\left[\frac{3\,n\,N_A}{4\pi V_m}\right]^{1/3} U_m$ (12)

Where $U_m$mean ultrasonic velocity

The value of mean ultrasonic velocity was calculated using relation [38].

It was found in our investigation that the elastic properties of the glass ceramics demonstrated a considerable advancement in comparison to the elastic properties of glass that were investigated in our earlier research[40].

$$U_m = \left[\frac{\left(\frac{1}{v_l^3}\right)+\left(\frac{2}{v_s^3}\right)}{3}\right]^{1/3} \quad (13)$$

Table 2 Values of Poisson's ratio, microhardness, thermal expansion coefficient and Debye temperature of the studied GC

Sample	δ	H (GP_a)	αp	θ_D (k)
$BBTD_{GC}0$	0.30449	8.4191	125614.6	480.76
$BBTD_{GC}0.25$	0.30338	8.6700	126101.8	485.21
$BBTD_{GC}0.5$	0.30106	9.1081	127053.0	492.807
$BBTD_{GC}0.75$	0.30014	9.4908	127841.8	499.357
$BBTD_{GC}1.00$	0.29414	10.0302	128839.4	504.989
$BBTD_{GC}1.25$	0.29951	10.0842	129605.0	509.485

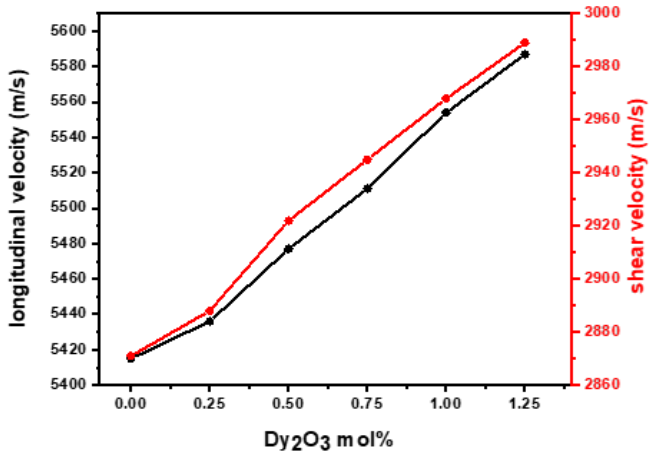

Figure 14 Variation of vl and vs against D_2O_3 contents for GC

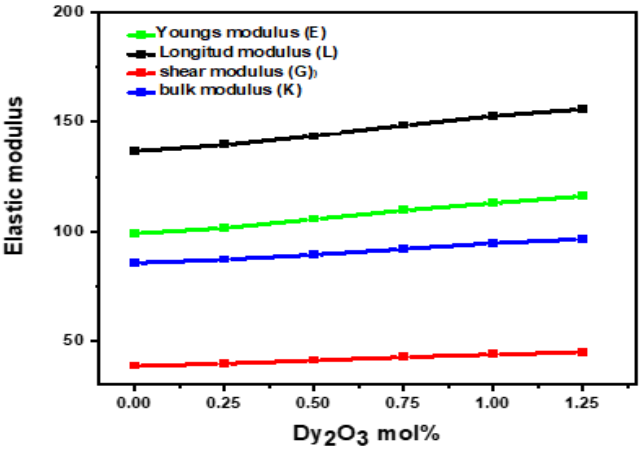

Figure 15 Variation of elastic modulus against D_2O_3 contents for GC

3.5 Gamma Radiation Shielding Capacity of GC

This study used a thallium doped sodium iodide detector for measuring the gamma radiation exposure Figure16. To determine the interaction probability of gamma ray photons with a material, we rely on a crucial gamma ray shielding parameter known as MAC (μ/ρ), measured in cm^2/g, with μ representing the linear attenuation coefficient, LAC). When an attenuator material is positioned between the source and detector, the primary intensity of gamma rays diminishes exponentially in accordance with the Beer-Lambert law written as [41, 42] $I = I_\circ\, e^{-\mu x}$, where $I_\circ$& I represent the incoming and outgoing intensity of gamma rays respectively, while x signifies the thickness of the glass attenuator.

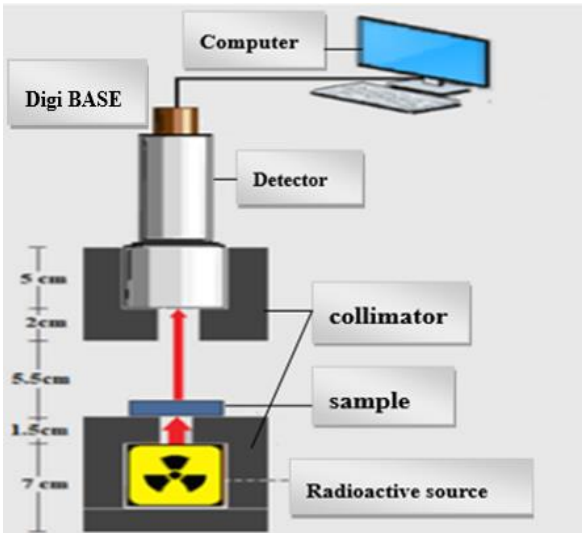

Figure 16 Schematic diagram of gamma ray spectrometer detector made of sodium iodide doped with thallium

Radioactive ^{137}Cs and ^{60}Co were used to generate the gamma rays with energies 0.662, 1.173 and 1.333 MeV.The parameter MAC of any material characterizes its capacity to protect against gamma rays exposure, quantifying the likelihood of photons being absorbed as they pass through a shielding material. The GC MAC values were o calculated using [43]:

$$\frac{\mu}{\rho} = \sum_i w_i \left(\frac{\mu}{\rho_i}\right) \quad (14)$$

Where ρ is represented is density, μ the linear attenuation coefficient.

Figure 17 shows the experimentally measured μ/ρ values against $h\nu$ of the GC, wherein the attenuation ability was decreased with the raise of photons energy. In addition, the MAC values were increased with the increase of Dy_2O_3 level and increasing heat treatmeant in the GC. essentially, substitution of B_2O_3 with Dy_2O_3 caused an enhancement in the GC density from 4.661 - 4.994 $g.cm^{-3}$, thus increasing the MAC values [44]. $BBTD_{GC}1.25$ showed the best MAC value. The figure clearly shows that the linear attenuation coefficient peaks at the lowest energy of gamma rays 0.662 MeV and then declines as the energy increases, reaching its minimum value at 1.333 MeV. As the photon energy increases, it is expected that the LAC & MAC values will decrease for all the prepared samples. This occurs because when the energy is increased, the probability of the photoelectric effect reaction, which is more prevalent at lower energies, decreases, and in turn, we observe the appearance of the Compton scattering reaction in the medium energy range. The parameter values start decreasing once the energy exceeds 1.173 MeV, as the pair production[45].

The values of half value layer HVL represent the material's depth that can attenuate 50% of the incident photon energy. The HVL values of the studied GC were calculated in terms of the linear attenuation coefficient μ via [46]:

$$HVL = \frac{0.693}{\mu} \quad (15)$$

Figures 18, 19 and 20 show the corresponding variation of *the* HVL, TVL *and* MFP values against $h\nu$ for the studied GC. Both *half value layer* HVL and tenth value layer TVL and are crucial in determining the shielding effectiveness of the synthesized GC against hazardous radiation [47]. The TVL thickness of a shielding or absorbing material necessary to decrease the radiation level by a factor of one-tenth. The TVL values of the proposed GC were estimated using:

$$TVL = \frac{ln10}{\mu} \quad (16)$$

The mean free path (MFP) is a measure of how far a gamma photon can travel before it undergoes an interaction. It is defined as the average distance between two consecutive gamma photon interactions. Generally, the MFP values of a shielding material can be affected by different factor like the kind of gamma ray photon energies, material's elemental composition and density and the radiation-matter interaction mechanisms. The MFP was calculated from MFP = (1/μ). It is an important parameter in radiation shielding and radiation detection, as it helps determine the effectiveness of materials in attenuating or absorbing gamma radiation.[48]. The density of the material has an inverse relationship with both MFP, HVL and TVL values[49]. Hence, it is concluded that the sample containing BBTDGC1.25 exhibits the lowest MFP and HVL values, indicating superior gamma ray protection capability. The values of MFP, TVL, and HVL are all measures of the penetration power of gamma photons through a material. A low value for any of these parameters indicates that gamma photons are more likely to interact with the glass sample, rather than passing through it. This suggests that the glass has a higher probability of absorbing or scattering gamma photons, resulting in better shielding performance. In practical terms, this means that the glass ceramic sample can effectively block or attenuate the transmission of gamma radiation, making it an ideal material for shielding applications in diverse industries including nuclear reactors, and medical facilities like radiography. The small values of these parameters for the GC are significant in determining its ability to provide efficient radiation protection [7]. The results of the study on glass ceramics showed a significant improvement in the ability to attenuate gamma rays, surpassing previous our research we conducted on glass [50].

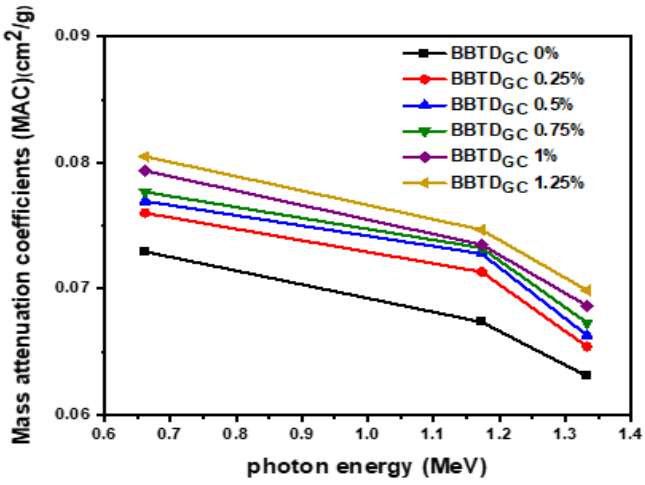

Figure 17 Variation of MAC values of the GC vs photon energy

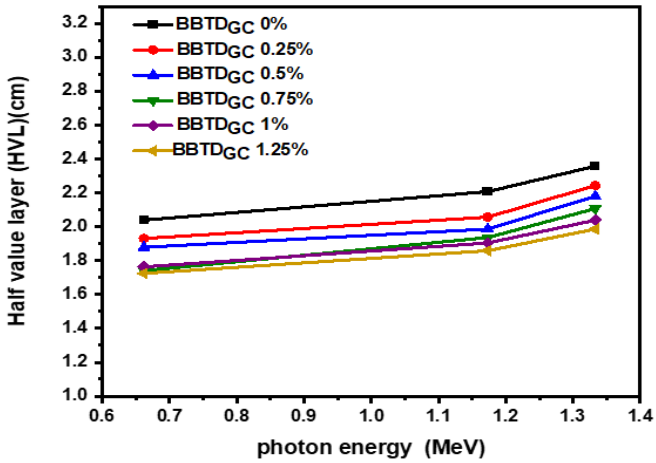

Figure 18 Chang of HVL values of the GC as a function of photon energy

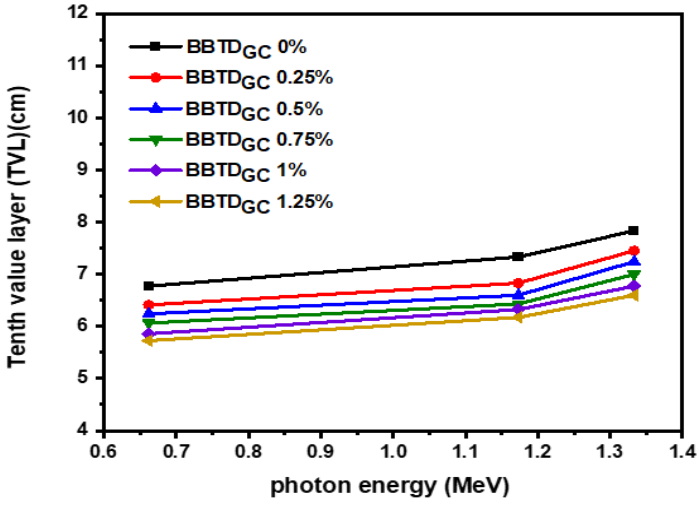

Figure 19 Chang of TVL values of the GC as a function of photon energy

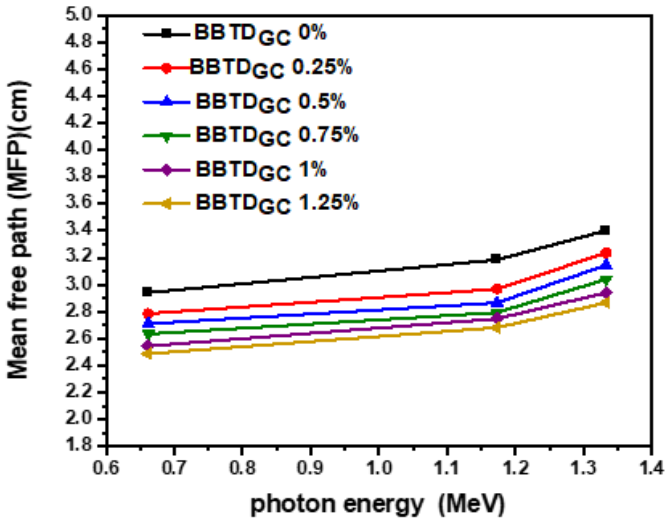

Figure 20 Changes of **MFP** values of the GC as a function of photon energy

4.0 CONCLUSION

A new type of gamma ray shielding GC composed of (50-x)B_2O_3-25TeO_2-25BaO-xDy_2O_3 were made from melt-quenching route and characterized using diverse analytical methods. The concentration (x) of Dy_2O_3 were changed from 0-1.25 mol% to tailor the structure, morphology, mechanical,and gamma ray shielding properties of the synthesized GC. Radioactive ^{137}Cs and ^{60}Co were used to generate the gamma rays with energies 0.662, 1.173 and 1.333 MeV for exposing the GC, determining their shielding capacity using a (NaI)Tl detector. These Dy_2O_3–doped GC showed excellent gamma rays shielding potency with the improvement of HVL, MAC, TVL and MFP values when Dy_2O_3 contents were increased with increasing heat treatment , which was mainly due to the increase of their network compactness (density was increased from 4.661 - 4.994 g.cm^{-3}). The obtained GC showed the expected elemental compositions and various crystalline phases with matched JCPDS card number. The improvement of the GC mechanical traits with the increase of Dy_2O_3 contents clearly indicated their strength enhancement and suitability to use against high energy gamma ray photons. It was affirmed that GC made with 1.25 mol% Dy_2O_3 can be the best shield against gamma ray exposure.

Acknowledgement

The authors appreciate the project's assistance and encouragement from Dr.Eslam Syala Department of Material Science, Institute of Graduate Studies and Researches, Alexandria University, National institute of standards cairo, Egypt and the Department of Physics, College of Science, Wasit University, Kut, Iraq.

Conflicts of Interest

The author declares that there is no conflict of interest regarding the publication of this paper.

References

[1] M. I. Sayyed, F. Akman, M. R. Kaçal, and A. Kumar. 2019. Radiation Protective Qualities of Some Selected Lead and Bismuth Salts in the Wide Gamma Energy Region. *Nuclear Engineering and Technology*. 51(3): 860–866. Doi: https://doi.org/10.1016/j.net.2018.12.018.

[2] M. Dolhen *et al.* 2020. A Comprehensive Study of the Glass/translucent Anti-glass/transparent Ceramic Structural Ordering in the $Bi_2O_3Nb_2O_5$–TeO_2 System. *Acta Materialia*. 189: 73–84.

[3] M. Naftaly and A. Jha. 2000. Nd 3+-doped Fluoroaluminate Glasses for a 1.3 μm Amplifier. *Journal of Applied Physics*. 87(5): 2098–2104.

[4] L. Koudelka, P. Mos, J. Pospís, L. Montagne, and G. Palavit. 2005. Structure and Properties of Titanium–zinc Borophosphate Glasses. *Journal of Solid State Chemistry*. 178(6): 1837–1843.

[5] L. R. Pinckney. 2001. Glass Ceramics. *Encyclopedia of Materials: Science and Technology*. K. H. J. Buschow *et al.* Eds. Oxford: Elsevier. 3535–3540.

[6] M. Y. Hanfi, A. K. Sakr, A. M. Ismail, B. M. Atia, M. S. Alqahtani, and K. A. Mahmoud. 2023. Physical Characterization and Radiation Shielding Features of $B_2O_3As_2O_3$ Glass Ceramic. *Nuclear Engineering and Technology*. 55(1): 278–284. Doi: https://doi.org/10.1016/j.net.2022.09.006.

[7] G. Susoy. 2020. Effect of TeO_2 Additions on Nuclear Radiation Shielding Behavior of Li_2O–B_2O_3–P_2O_5–TeO_2 Glass-system. *Ceramics International*. 46(3): 3844–3854.

[8] F. B. Costa, K. Yukimitu, L. A. O. Nunes, L. H. d. C. Andrade, S. M. Lima, and J. C. S. Moraes. 2015. Characterization of Nd3+-Doped Tellurite Glasses with Low OH Content. *Materials Research*. 18: 2–7.

[9] H. Nii, K. Ozaki, M. Herren, and M. Morita. 1998. Up-conversion Fluorescence of Er3+—and Yb3+-doped TeO_2-based Oxide Glass and Single Crystals. *Journal of luminescence*. 76: 116–119.

[10] P. Pascuta *et al.* 2019. The impact of Ag and Cu Nanoparticles on Optical and Magnetic Properties of New Tb_2O_3-PbO-TeO_2 Glass Ceramic System. *Journal of Alloys and Compounds*. 799: 442–449.

[11] S. D. Stookey. 1959. Catalyzed Crystallization of Glass in Theory and Practice. *Industrial & Engineering Chemistry*. 51(7): 805–808. Doi: 10.1021/ie50595a022.

[12] R. Siripuram, P. Rao, and S. Sripada. 2022. Comparative Studies of Structural and Optical Properties of Nb_2O_5–Sb_2O_3–TeO_2 Glass and Glassceramics. *Physics and Chemistry of Glasses-European Journal of Glass Science and Technology Part B*. 63(3): 65–85.

[13] I. Boukhris, M. S. Al-Buriahi, H. Akyildirim, A. Alalawi, I. Kebaili, and M. I. Sayyed. 2020. Chalcogenide Glass-ceramics for Radiation Shielding Applications. *Ceramics International*. 46(11, Part B): 19385–19392, Doi: https://doi.org/10.1016/j.ceramint.2020.04.281.

[14] A. Araz, E. Kavaz, and R. Durak. 2021. Neutron and Photon Shielding Competences of Aluminum Open-cell Foams Filled with Different Epoxy Mixtures: An Experimental Study. *Radiation Physics and Chemistry*. 182: 109382. Doi: https://doi.org/10.1016/j.radphyschem.2021.109382.

[15] M. Środa, S. Świontek, and D. Fraś. 2019. Effect of Ga_2O_3 on the Structure and Properties of TeO_2–GeO_2 Glass Doped with Pr^{3+}. *Journal of Non-Crystalline Solids*. 526: 119699. Doi: https://doi.org/10.1016/j.jnoncrysol.2019.119699.

[16] M. Cai, B. Zhou, Y. Tian, J. Zhou, S. Xu, and J. Zhang. 2016. Broadband Mid-infrared 2.8μm Emission in Ho^{3+}/Yb^{3+}-Codoped Germanate Glasses. *Journal of Luminescence*.

171: 143–148. Doi: https://doi.org/10.1016/j.jlumin.2015.11.016.
[17] S. N. Nazrin *et al.* 2018. The Effect of Erbium Oxide in Physical and Structural Properties of Zinc Tellurite Glass System. *Journal of Non-Crystalline Solids*. 490: 35–43. Doi: https://doi.org/10.1016/j.jnoncrysol.2018.03.017.
[18] S. A. Tijani *et al.* 2018. Radiation Shielding Properties of Transparent Erbium Zinc Tellurite Glass System Determined at Medical Diagnostic Energies. *Journal of Alloys and Compounds*. 741: 293–299. Doi: https://doi.org/10.1016/j.jallcom.2018.01.109.
[19] M. Kamislioglu, E. E. Altunsoy Guclu, and H. O. Tekin. 2020. Comparative Evaluation of Nuclear Radiation Shielding Properties of $xTeO_{2+}$ (100–x)Li_2O Glass System. *Applied Physics A*. 126(2): 95. Doi: 10.1007/s00339-020-3284-3.
[20] J. E. Stanworth. 1950. *Physical properties of Glass*. The Clarendon Press, Oxford.
[21] K. A. Matori, M. I. Sayyed, H. A. A. Sidek, M. H. M. Zaid, and V. P. Singh. 2017. Comprehensive Study on Physical, Elastic and Shielding Properties of Lead Zinc Phosphate Glasses. *Journal of Non-Crystalline Solids*. 457: 97–103. Doi: https://doi.org/10.1016/j.jnoncrysol.2016.11.029.
[22] M. Çelikbilek, A. E. Ersundu, and S. Aydin. 2013. Preparation and Characterization of TeO_2–WO_3–Li_2O Glasses. *Journal of Non-Crystalline Solids*. 378: 247–253. Doi: https://doi.org/10.1016/j.jnoncrysol.2013.07.020.
[23] K. A. Mahmoud, F. I. El-Agwany, Y. S. Rammah, and O. L. Tashlykov. 2020. Gamma Ray Shielding Capacity and Build Up Factors of CdO Doped Lithium Borate Glasses: Theoretical And Simulation Study. *Journal of Non-Crystalline Solids*. 541: 120110. Doi: https://doi.org/10.1016/j.jnoncrysol.2020.120110.
[24] M. Faragl, M. El-Okrl, R. Mahanill, G. Turkyll, and H. Afifyll. 2014. Investigation of Dielectric and Optical Properties of MgO Thin Films. *Int. J. Adv. Eng., Technol. Comput. Sci.* 1(1): 1–9.
[25] R. El-Mallawany. 2018. *Tellurite Glass Smart Materials: Applications in Optics and Beyond*. Springer,
[26] S. Djambazov, V. Dimitrov, and R. Iordanova. 2017. In Memoriam: Yanko Borisov Dimitriev, 1937–2016. *Journal of Non Crystalline Solids*. 470: 194–194.
[27] S. F. Hathot, N. J. Jubier, R. H. Hassani, and A. Salim. 2021. Physical and Elastic Properties of TeO_2-Gd_2O_3 Glasses: Role of Zinc Oxide Contents Variation. *Optik*. 247: 167941.
[28] W. M. Haynes. 2014. *CRC Handbook of Chemistry and Physics*. CRC Press.
[29] D. Yin, F. Yang, L. Wu, Y. Zhou, H. Zhou, and X. Wang. 2015. Enhanced 2.7 μm Mid-infrared Emission and Energy Transfer Mechanism in Er^{3+}/Nd^{3+} Codoped Tellurite Glass. *Journal of Alloys and Compounds*. 618: 666–672.
[30] S. Kawasaki, T. Honma, Y. Benino, T. Fujiwara, R. Sato, and T. Komatsu. 2003. Writing of Crystal-dots and Lines by YAG Laser Irradiation and Their Morphologies in Samarium Tellurite Glasses. *Journal of Non-Crystalline Solids*. 325(1–3): 61–69.
[31] H. Sidek, S. Rosmawati, B. Azmi, and A. Shaari. 2013. Effect of ZnO on the Thermal Properties of Tellurite Glass. *Advances in Condensed Matter Physics*.
[32] S. Xiang, N. Qiuhua, X. Tiefeng, D. Shixun, and W. Xunsi. 2008. Investigation on Energy Transfer from Er^{3+} to Nd^{3+} in Tellurite Glass. *Journal of Rare Earths*. 26(6): 899–903.
[33] M. Sobczyk. 2013. Temperature-dependent Luminescence and Temperature-stimulated NIR-to-VIS up-conversion in Nd^{3+}-doped La_2O_3–Na_2O–ZnO–TeO_2 Glasses. *Journal of Quantitative Spectroscopy and Radiative Transfer*. 119: 128–136.
[34] S. S. Babu *et al.* 2010. Spectroscopic Investigations of 1.06 μm Emission in Nd3+-doped Alkali Niobium Zinc Tellurite Glasses. *Journal of Luminescence*. 130(6): 1021–1025.
[35] A. Hrubý. 1972. Evaluation of Glass-forming Tendency by Means of DTA. *Czechoslovak Journal of Physics B*. 22(1): 1187–1193.
[36] J. D. Mackenzie. 1987. Applications of Zachariasen's Rules to Different Types of Noncrystalline Solids. *Journal of Non-Crystalline Solids*. 95: 441–448.
[37] A. F. A. El-Rehim, E. A. A. Wahab, M. M. A. Halaka, and K. S. Shaaban. 2022. Optical Properties of SiO_2 – TiO_2 – La_2O_3 – Na_2O – Y_2O_3 Glasses and a Novel Process of Preparing the Parent Glass-Ceramics. *Silicon*. 14(2): 373–384. Doi: 10.1007/s12633-021-01002-w.
[38] M. Halimah *et al.* 2005. Ultrasonic Study and Physical Properties of Borotellurite Glasses. *Am. J. Appl. Sci*. 2(11): 1541–6.
[39] R. El-Mallawany, H. Afifi, M. El-Gazery, and A. Ali. 2018. Effect of Bi_2O_3 Addition on the Ultrasonic Properties of Pentaternary Borate Glasses. *Measurement*. 116: 314–317.
[40] S. F. Hathot, B. M. Al dabbagh, and H. Aboud. 2024. Effects of Dy_2O_3 Doping on Physical and Mechanical Characteristics of B_2O_3-TeO_2-BaO Glass. *Engineering and Technology Journal*. 1–10. Doi: 10.30684/etj.2024.145037.1649.
[41] A. M. A. Mostafa *et al.* 2021. PbO–Sb_2O_3–B_2O_3–CuO Glassy System: Evaluation of Optical, Gamma and Neutron Shielding Properties. *Materials Chemistry and Physics*. 258: 123937. Doi: https://doi.org/10.1016/j.matchemphys.2020.123937.
[42] H. O. Tekin, V. P. Singh, and T. Manici. 2017. Effects of Micro-sized and Nano-sized WO3 on Mass Attenauation Coefficients of Concrete by using MCNPX Code. *Applied Radiation and Isotopes*. 121: 122–125. Doi: https://doi.org/10.1016/j.apradiso.2016.12.040.
[43] F. Akman, M. Kaçal, M. Sayyed, and H. Karataş. 2019. Study of Gamma Radiation Attenuation Properties of Some Selected Ternary Alloys. *Journal of Alloys and Compounds*. 782: 315–322.
[44] Y. Al-Hadeethi and M. I. Sayyed. 2020. A Comprehensive Study on the Effect of TeO_2 on the Radiation Shielding Properties of TeO_2–B_2O_3–Bi_2O_3–LiF–$SrCl_2$ Glass System using Phy-X/PSD Software. *Ceramics International*. 46(5): 6136–6140. Doi: https://doi.org/10.1016/j.ceramint.2019.11.078.
[45] S. Yin, H. Wang, S. Wang, J. Zhang, and Y. Zhu. 2022. Effect of B_2O_3 on the Radiation Shielding Performance of Telluride Lead Glass System. *Crystals*. 12(2): 178.
[46] M. Almatari, O. Agar, E. E. Altunsoy, O. Kilicoglu, M. I. Sayyed, and H. O. Tekin. 2019. Photon and Neutron Shielding Characteristics of samarium Doped Lead Alumino Borate Glasses Containing Barium, Lithium and Zinc Oxides Determined at Medical Diagnostic Energies. *Results in Physics*. 12: 2123–2128. Doi: https://doi.org/10.1016/j.rinp.2019.01.094.
[47] R. El-Mallawany, M. Sayyed, and M. Dong. 2017. Comparative Shielding Properties of Some Tellurite Glasses: Part 2, *Journal of Non-Crystalline Solids*. 474: 16–23.
[48] O. Agar, H. O. Tekin, M. I. Sayyed, M. E. Korkmaz, O. Culfa, and C. Ertugay. 2019. Experimental Investigation of Photon Attenuation Behaviors for Concretes Including Natural Perlite Mineral. *Results in Physics*. 12: 237–243. Doi: https://doi.org/10.1016/j.rinp.2018.11.053.
[49] S. Stalin *et al.* 2020. Structural, Optical Features and Gamma Ray Shielding Properties of Bi_2O_3–TeO_2–B_2O_3-GeO2 Glass System. *Ceramics International,* vol. 46, no. 11, Part A, pp. 17325-17334. Doi: https://doi.org/10.1016/j.ceramint.2020.04.021.
[50] S. Farhan, B. Al Dabbagh, and H. Aboud. 2024. Optical and Radiation Shielding Characteristics of Dy_2O_3 Doped B_2O_3–TeO_2–BaO Glasses. *Chalcogenide Letters*. 21(6): 459–473.